Monthly Notices of the ROYAL ASTRONOMICAL SOCIETY

MNRAS **509,** 1465–1477 (2022)
Advance Access publication 2021 September 21

https://doi.org/10.1093/mnras/stab2693

Regular and chaotic orbits in axisymmetric stellar systems

Raffaele Pascale [1,2★] Carlo Nipoti [2] and Luca Ciotti [2]

[1] *INAF - Osservatorio di Astrofisica e Scienza dello Spazio di Bologna, via Piero Gobetti 93/3, I-40129 Bologna, Italy*
[2] *Dipartimento di Fisica e Astronomia 'Augusto Righi', Università di Bologna, via Piero Gobetti 93/2, I-40129 Bologna, Italy*

Accepted 2021 September 15. Received 2021 September 14; in original form 2020 December 29

ABSTRACT

The gravitational potentials of realistic galaxy models are in general non-integrable, in the sense that they admit orbits that do not have three independent isolating integrals of motion and are therefore chaotic. However, if chaotic orbits are a small minority in a stellar system, it is expected that they have negligible impact on the main dynamical properties of the system. In this paper, we address the question of quantifying the importance of chaotic orbits in a stellar system, focusing, for simplicity, on axisymmetric systems. Chaotic orbits have been found in essentially all (non-Stäckel) axisymmetric gravitational potentials in which they have been looked for. Based on the analysis of the surfaces of section, we add new examples to those in the literature, finding chaotic orbits, as well as resonantly trapped orbits among regular orbits, in Miyamoto-Nagai, flattened logarithmic and shifted Plummer axisymmetric potentials. We define the fractional contributions in mass of chaotic (ξ_c) and resonantly trapped (ξ_t) orbits to a stellar system of given distribution function (DF), which are very useful quantities, for instance in the study of the dispersal of stellar streams of galaxy satellites. As a case study, we measure ξ_c and ξ_t in two axisymmetric stellar systems obtained by populating flattened logarithmic potentials with the Evans ergodic DF, finding $\xi_c \sim 10^{-4} - 10^{-3}$ and $\xi_t \sim 10^{-2} - 10^{-1}$.

Key words: chaos – methods: numerical – methods: statistical – celestial mechanics – galaxies: kinematics and dynamics.

1 INTRODUCTION

In stellar dynamics, the most important class of axisymmetric and triaxial gravitational potentials known to be integrable are those of the Stäckel (1893) family: the separability of the Hamilton–Jacobi equation in ellipsoidal coordinates ensures the existence of three global independent isolating integrals of motion and thus that all orbits are regular (see e.g. de Zeeuw 1985 and de Zeeuw & Lynden-Bell 1985). The gravitational potentials of realistic galactic models, which in general are not of Stäckel form, are not guaranteed to be integrable and can admit chaotic orbits, i.e. orbits that do not have three independent isolating integrals of motion. The integrability of non-spherical galactic potentials and the contribution of chaotic orbits to stellar systems with non-integrable potentials are important questions for galactic dynamics, which can be addressed by classifying samples of numerically integrated orbits.

In the present work, we focus on axisymmetric potentials. Though chaos is often studied in the context of triaxial potentials (e.g. Schwarzschild 1979, 1982; Miralda-Escude & Schwarzschild 1989; Valluri & Merritt 1998), chaotic orbits are also found in axisymmetric potentials (e.g. Henon & Heiles 1964; Hunter 2003, 2005; Zotos & Carpintero 2013). In fact, chaotic orbits have been found in essentially all (non-Stäckel) axisymmetric potentials in which they have been looked for. Hunter (2005) suggested that a possible exception could be the family of Miyamoto-Nagai (hereafter MN) potentials (Miyamoto & Nagai 1975), whose limiting cases – the Plummer (1911) sphere and the Kuzmin (1956) disc – are integrable, but it turns out this is not the case, because, as we show in this paper, the MN family admits chaotic orbits. Using the surface-of-section (SoS) method (Henon & Heiles 1964; Binney & Tremaine 2008), we add new examples to those previously considered in the literature, demonstrating that a few more families of axisymmetric potentials are non-integrable (at least for some values of their parameters): not only the aforementioned MN potential, but also the shifted Plummer axisymmetric and the flattened logarithmic potentials.

Of course, while it is sufficient to find a chaotic orbit to demonstrate that a given potential is non-integrable, it is impossible to proof with numerical integration of orbits that a given potential is integrable. However, for many practical purposes it is not so important to determine whether a given potential is integrable or not, but rather to estimate the fractional contribution of chaotic orbits to a stellar system. There is general consensus, mainly based on the results of numerical investigations (Schwarzschild 1979; Richstone 1982), that in realistic galactic potentials 'most of the orbits are regular' and that reasonable dynamical models can be built by neglecting the small fraction of chaotic orbits. However, especially in an era in which the galactic dynamical models are more and more sophisticated (e.g. Binney 2020) and the observational data are characterized by high resolution and high statistics (Kordopatis et al. 2013; Majewski et al. 2017; Gaia Collaboration 2018a,b, 2020), one would really like to make more quantitative statements about the relative contributions of regular and chaotic orbits. An astrophysical application in which the knowledge of these contributions is highly relevant is the study of stellar streams of galaxy satellites, often used as tracers of the host galaxy gravitational field and thus mass density distribution (Helmi & White 1999; Fardal, Huang & Weinberg 2015; Bonaca et al. 2020; Mestre, Llinares & Carpintero 2020). In essence, the time over which a stream is dispersed is expected to be much shorter if the

★ E-mail: raffaele.pascale@inaf.it

orbit of its progenitor satellite (globular cluster of dwarf galaxy) is chaotic than if it is regular. In some cases even orbits with extremely long characteristic chaotic time-scales can produce chaotic effects on relatively short time-scales (Price-Whelan et al. 2016).

Quantitative estimates of the fractional contributions of chaotic and regular orbits to stellar systems are rare in the literature. Maffione et al. (2015), extracting particles from solar neighbourhood-like volumes of dark-matter only cosmological simulations of Milky-Way like haloes, estimated the fractions of chaotic and regular orbits, integrated in triaxial analytic approximations of the simulated gravitational potentials. A similar systematic study was carried out by Maffione et al. (2018), who considered more realistic N-body realizations of Milky-Way-like galaxies extracted from hydrodynamic cosmological simulations. Here, adopting a non-cosmological, but fully self-consistent approach, we consider stellar systems with given distribution function (DF), for which we provide rigorous definitions of the fractional contributions in mass of regular and chaotic orbits.

Regular orbits include the special family of resonantly trapped orbits. While a resonant orbit is such that its fundamental frequencies are commensurable, an orbit is said to be *resonantly trapped* when it is, in phase space, close to a resonant orbit (see Binney & Tremaine 2008). Resonantly trapped orbits must be treated with special care, since they behave differently from the other regular orbits in the angle-action space (Binney 2016). Also the aforementioned dispersal of stellar streams can be significantly affected, or even dominated, by the presence of families of resonantly trapped orbits in the host gravitational field. The time over which a stream is dispersed can be relatively short if the orbit of the progenitor satellite is close to a separatrix, i.e. the boundary between two orbit families, each defined by a different orbital resonance (a phenomenon known as separatrix divergence; Yavetz et al. 2021). In the following, we will refer to regular orbits that are not resonantly trapped as *untrapped*. Thus, in addition to chaotic orbits, in this work, we also classify separately resonantly trapped and untrapped regular orbits, detecting them with the SoS method and measuring their fractional mass contributions to a stellar system.

As a case study, we present the results obtained by estimating the fractional contributions in mass of regular and chaotic orbits to flattened axisymmetric stellar systems with luminous component with Evans (1993) DF, embedded in an external logarithmic gravitational potential. Evans' models, though idealized in some respects (they are isotropic and they do not account explicitly for the self-gravity of the luminous component), are interesting for applications in galactic dynamics, because their luminous density distribution is, for a range of values of their free parameters, a reasonably good model of the luminous density distribution of galactic spheroids. The flattened axisymmetric logarithmic potential has been widely used in applications to galactic dynamics: gravitational potentials belonging to this family has been adopted, for instance, by Helmi (2004a) and Helmi (2004b) to model the dark matter halo of the Milky Way, by Bovy (2014) to study tidal streams, and by Sanders et al. (2016) to model dark matter haloes of dwarf spheroidal galaxies. More recently, Hagen, Helmi & Breddels (2019) used Evans models to build mock dwarf spheroidal galaxy models.

The paper is organized as follows. After recalling the definition of the SoS in Section 2 and describing the adopted numerical methods in Section 3, in Section 4 we present new results on SoS-based classification of orbits in axisymmetric potentials. In Section 5, we define the fractional mass contributions of regular and chaotic orbits to a stellar system with given DF, and we present the results of our case study. Section 6 concludes.

2 SURFACES OF SECTION FOR ORBITS IN AXISYMMETRIC POTENTIALS

Let $\Phi(R, z)$ be an axisymmetric potential in cylindrical coordinates (R, ϕ, z), and let γ be the trajectory in phase space of a star moving under the action of Φ. The Poincaré map or SoS is the plane having (R, p_R) as axes, where p_R is the momentum conjugated to R. The trace of an orbit in the SoS is the set of the orbit's consequents, i.e. the points with coordinates (R, p_R) defined by the intersections of γ with the equatorial plane ($z = 0$). Potentials that are time-independent and invariant with respect to rotation around a given axis (chosen to be the z-direction) admit as global integrals of motion the specific (i.e. per unit mass) energy E and the z-component of the specific angular momentum L_z. For given E and L_z, the points of a trace belong, by construction, to the manifold defined by the implicit function

$$E = \frac{1}{2}\left(p_R^2 + p_z^2\right) + \Phi_{\rm eff}\,(R, 0), \tag{1}$$

where p_z is the momentum conjugated to z and

$$\Phi_{\rm eff}(R, z) = \frac{L_z^2}{2R^2} + \Phi(R, z) \tag{2}$$

is the effective potential.

While the manifold (1) is 2D, the trace of an orbit in the SoS can be either 1D or 2D. For given E and L_z, the consequents of an orbit are confined to a region which is given by the relation

$$E - \Phi_{\rm eff}(R, 0) \geq 0. \tag{3}$$

Also, traces of different orbits with the same values of E and L_z cannot cross each other in the SoS: if the traces of two orbits intersected at one or more points in the SoS, there would exist a point on γ where the two orbits have the same (E, L_z, R, p_R) at $z = 0$. Thus, the two orbits would have the same trajectory, because equation (1) implies that they could only differ in the sign of p_z. The sign ambiguity is usually resolved by tracing a point on the SoS only when the crossing of the equatorial plane occurs with $p_z > 0$. Here, we do not conform to this convention but, as done for instance in Richstone (1982) and Hunter (2005), we trace a point in the SoS for crossings with both $p_z > 0$ and $p_z < 0$. We find this choice convenient because, following Richstone (1982), we then classify an orbit as resonantly trapped if its trace in the SoS consists of two or more unconnected loops.

For axially symmetric potentials, given a trace of consequents, the existence of a third isolating integral is deduced by the dimensionality of the trace in the SoS. A 1D trace implies that the motion is further constrained on to an additional surface, defined, for instance, by $p_R = p_R(R, z, p_z)$, leading to the conclusion that the orbit is regular. Instead, when there is no additional integral of motion, the consequents populate 2D regions of the SoS and the orbit is chaotic. SoS have been used to study the existence of a third isolating integral since the mid 1960s (e.g. Henon & Heiles 1964; Bienaymé, Robin & Famaey 2015).

3 NUMERICAL METHODS

Before presenting the results obtained applying the SoS method to classify orbits in a few axisymmetric potentials (Sections 4 and 5), we describe here the adopted numerical tools that allow us to obtain the required accuracy in the computation of the orbits' traces in the SoS.

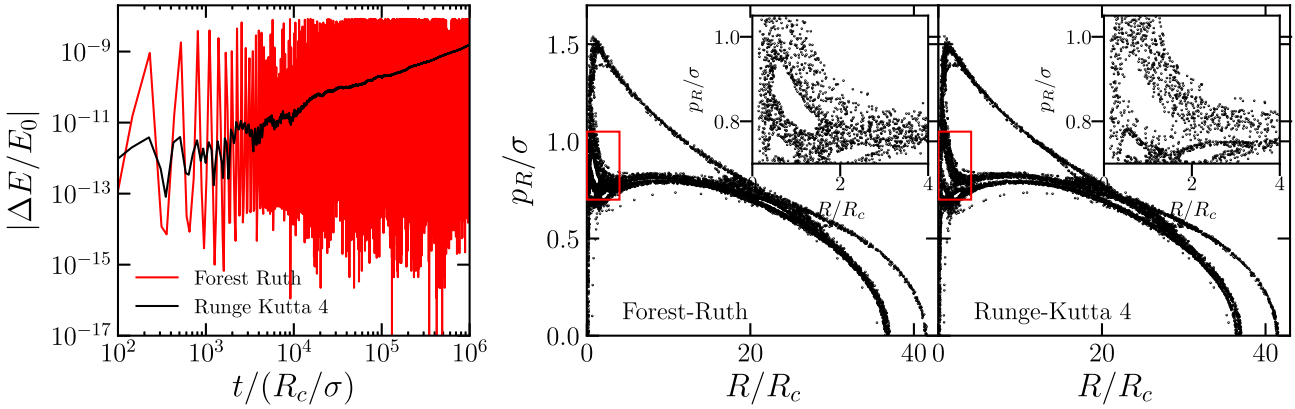

Figure 1. Left-hand panel: relative energy variation as a function of time for a chaotic orbit integrated in the potential (23) with $q = 0.75$ and $R_c = \sigma = 1$, using the symplectic Forest–Ruth algorithm (red curve) and the RK 4 scheme (black curve) described in Section 3.1. Middle panel: trace in the SoS of the same orbit as in the left-hand panel integrated with the Forest-Ruth scheme. Right-hand panel: same as the middle panel, but using the adaptive RK 4 scheme. The small insets in the middle and right-hand panels show zoomed-in views of the red boxes in the corresponding main panels.

3.1 Numerical integration of the orbits

As done in other works on orbit classification in galactic potentials (e.g. Richstone 1982; Price-Whelan et al. 2016), we opted for a Runge–Kutta (RK) algorithm to integrate numerically the equations of motion. Specifically, we computed the orbits using an adaptive fourth-order RK integrator (hereafter RK 4; Butcher 1996). The integration is performed in Cartesian coordinates according to the following scheme (Press & Teukolsky 1992):

(i) Let $\mathbf{w} = (x, y, z, v_x, v_y, v_z)$. Starting from the phase-space position $\mathbf{w}_n$ at a time t_n, we evaluate the proposals $\mathbf{w}_{n+1}^{\Delta t_n}$ and $\mathbf{w}_{n+1}^{\Delta t_n/2}$ at a subsequent time t_{n+1}, corresponding, respectively, to time steps Δt_n and $\Delta t_n/2$.

(ii) We evaluate $\epsilon_n = \max_i |1 - w_{n+1,i}^{\Delta t_n}/w_{n+1,i}^{\Delta t_n/2}|$ and compare it to some predetermined accuracy ϵ. $w_{n+1,i}^{\Delta t_n}$ and $w_{n+1,i}^{\Delta t_n/2}$, with $i = 1, ..., 6$, are the i-th elements of the vectors $\mathbf{w}_{n+1}^{\Delta t_n}$ and $\mathbf{w}_{n+1}^{\Delta t_n/2}$, respectively.

(a) If $\epsilon_n > \epsilon$, both proposals $\mathbf{w}_{n+1}^{\Delta t_n}$ and $\mathbf{w}_{n+1}^{\Delta t_n/2}$ are rejected, and new proposals for $\mathbf{w}_{n+1}^{\Delta t_n}$ and $\mathbf{w}_{n+1}^{\Delta t_n/2}$ are found using as new time step

$$\Delta t_n \beta (\epsilon/\epsilon_n)^{1/(h+1)}, \tag{4}$$

and its half, respectively, where β and ϵ are dimensionless parameters, and $h = 4$ is the order of the RK scheme.

(b) If $\epsilon_n < \epsilon$, $\mathbf{w}_{n+1} = \mathbf{w}_{n+1}^{\Delta t_n/2}$ and the new timestep is

$$\Delta t_n \beta (\epsilon/\epsilon_n)^{1/h}. \tag{5}$$

RK algorithms are known to be dissipative, in the sense that they do not ensure the conservation of the mechanical energy in a Hamiltonian system. As shown for instance by Stuchi (2002), if the numerical integration of a test particle in a Hamiltonian system proceeds for sufficiently long time, when using dissipative algorithms the energy drifts because of numerical dissipation and the consequent deviation of the integrated phase-space position from the true one can in principle shift the target particle from a region of regularity to a region of chaos. This can make an intrinsically regular orbit appear as chaotic after a long-time integration. For this reason, in the context of numerical integration of orbits and their classification as regular or chaotic, it is sometimes preferred the use of symplectic integrators, which are not dissipative (e.g. Barnes 2001; Mestre et al. 2020).

Our adaptive RK scheme implementation allows us to keep very high precision in the orbit integration and minimize numerical dissipation. In equations (4 and 5), we set $\beta = 0.9$ and $\epsilon = 10^{-12}$, obtaining energy conservation of a part over $10^{12} - 10^{9}$, depending on the maximum time integration required, which is a strong indication that the effects of dissipation should be negligible. As an additional check that our results are not significantly affected by numerical effects related to accuracy and the dissipative nature of the adopted integrator, we integrated all the orbits classified as chaotic based on the RK 4 integration with $\epsilon = 10^{-12}$, also requiring $\epsilon = 10^{-15}$ in equations (4 and 5), and also with the fourth order symplectic Forest-Ruth integrator (Forest & Ruth 1990; Yoshida 1990; Candy & Rozmus 1991), finding very good agreement between the numerical results and confirming the classification. In Fig. 1, we compare the relative energy variation of a chaotic orbit integrated in the potential (23) using our implementation of the RK 4 scheme and the aforementioned symplectic Forest-Ruth scheme. Although the RK scheme introduces numerical dissipation, the energy drift is always comparable with the energy oscillations produced by the Forest-Ruth scheme and, as shown in the middle and right-hand panels of Fig. 1, the orbit manifests its chaotic behaviour when integrated with both algorithms. In terms of time performance, our implementation of the adaptive RK 4 scheme is 1.5–7 times faster than the considered Forest-Ruth scheme (depending on the specific orbit) and allows us to evaluate very precisely the phase-space coordinates at the times of crossing of the equatorial plane (see Section 3.2).

3.2 Computation of the traces in the surface of section

Central to evaluate consequents in the SoS is the ability to compute as precisely as possible $\mathbf{w}$ at the time corresponding to each crossing of the equatorial plane. Each time $z_n z_{n+1} < 0$ (i.e. a crossing through the equatorial plane has occurred), together with equations (4 and 5), we make the further requirement that $|z_{n+1} - z_n|/R_0 < \varepsilon_z$, where R_0 is a characteristic radius, for instance $R_0 \equiv R_c$ in case of the logarithmic potential of Section 5.2. When the condition is not satisfied a new guess for z_{n+1} is made halving the time step. Such condition ensures that z_{n+1} is close to the equatorial plane to a precision dictated by ε_z. Throughout this work, we have adopted $\varepsilon_z = 10^{-6}$. In Fig. 2, we show the consequents in the SoS of an orbit integrated in the potential (23) using $\varepsilon_z = 10^{-1}$ (left-hand panel) and $\varepsilon_z = 10^{-6}$ (right-hand panel). The traces belong to a regular trapped orbit (see also Section 4.1), whose loops are so tight in the SoS that, if the crossings of the equatorial plane are not precisely evaluated (as in

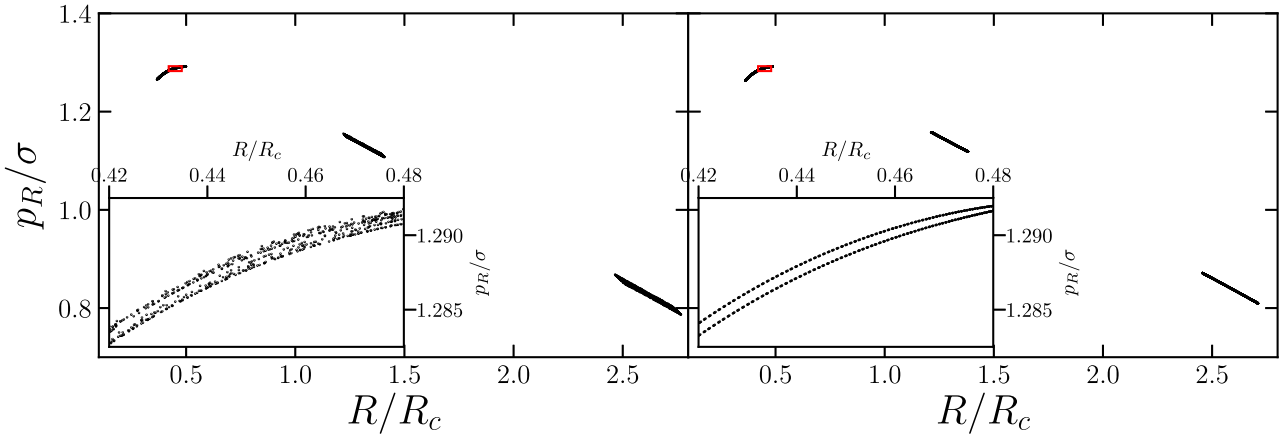

Figure 2. Left-hand panel: trace in the SoS of a test resonantly trapped orbit integrated in the potential (23) whose crossings of the equatorial plane have been evaluated using $\varepsilon_z = 10^{-1}$. Right-hand panel: same as the left-hand panel, but with $\varepsilon_z = 10^{-6}$.

the left-hand panel), the orbit could be misclassified as chaotic. The inset in the right-hand panel of Fig. 2 demonstrates that the choice $\varepsilon_z = 10^{-6}$ guarantees the required accuracy.

4 FINDING CHAOTIC ORBITS IN AXISYMMETRIC GRAVITATIONAL POTENTIALS

Here, we apply the SoS method to classify orbits in two families of axisymmetric potentials: the shifted Plummer and MN potentials. Orbits in the shifted Plummer potentials, as far as we are aware, have not been studied before. Orbits in a MN potential have been classified by Hunter (2005) and Zotos & Carpintero (2013), who found only regular orbits (see also Greiner 1987, 1990). In Sections 4.1 and 4.2, we present examples of potentials belonging to these families, showing that they admit, together with regular orbits, also chaotic orbits. Among regular orbits, we identify also members of the special family of resonantly trapped orbits. A third family of gravitational potentials, the flattened axisymmetric logarithmic potentials (Binney 1981), is considered in Section 5.2. Orbits in these logarithmic potentials have been studied in previous works (Richstone 1982; Barnes 2001), but, to our knowledge, only regular orbits have been found so far: in Section 5.2, we show examples of chaotic orbits in two potentials of this family.

4.1 Orbits in a shifted Plummer potential

The complexification is a shift $\mathbf{x} \to \mathbf{x} - \mathrm{i}\mathbf{a}$ that maps a potential $\Phi(\mathbf{x})$ into $\Phi(\mathbf{x} - \mathrm{i}\mathbf{a})$, where $\mathbf{a} = (a_1, a_2, a_3)$ is a triplet of real numbers. As shown by Ciotti & Giampieri (2007) and Ciotti & Marinacci (2008), the complex shift method can be used to obtain analytic density–potential pairs (ρ, Φ) for axisymmetric models starting from spherical ones. If Φ satisfies the Poisson equation $\nabla^2\Phi = 4\pi G\rho$ with analytic Φ and ρ, thanks to the linearity of the shift and of the Poisson equation, the shift gives birth to two analytic density–potential pairs given by the real and complex parts of $\Phi(\mathbf{x} - \mathrm{i}\mathbf{a})$ and $\rho(\mathbf{x} - \mathrm{i}\mathbf{a})$. The method was first introduced in electrostatics by Appell (1887), Whittaker & Watson (1950), Carter (1968), and others, and later applied to gravitational potentials (Ciotti & Giampieri 2007, Ciotti & Marinacci 2008, and reference therein). The complex shift method is of special interest for the purposes of this work. It is, for instance, reasonable to speculate that during the complexification of a spherical potential some of the integrability properties are transferred to the complexified versions, as shown by the surprising integrability properties of the complexified point-mass potential (Lynden-Bell 1962, 2000, 2003).

Following Ciotti & Giampieri (2007), let us consider the gravitational potential

$$\Phi(R, z) = -\frac{GM}{b}\psi(R, z), \tag{6}$$

where

$$\psi(R, z) = \sqrt{\frac{d + 1 + \tilde{r}^2 - \tilde{a}^2}{2d^2}}, \tag{7}$$

with

$$d = \sqrt{\left(1 - \tilde{a}^2 + \tilde{r}^2\right)^2 + 4\tilde{a}^2\tilde{z}^2}. \tag{8}$$

Here $\tilde{R} \equiv R/b$, $\tilde{z} \equiv z/b$, $\tilde{a} \equiv a/b$, and $\tilde{r}^2 = \tilde{R}^2 + \tilde{z}^2$. Known as shifted Plummer model, the axisymmetric potential (6) is obtained by means of the complexification of a classical Plummer (1911) sphere with mass M and core radius b. The potential (6) corresponds to the real part of the shift of the spherical Plummer model, with $\mathbf{a} = (0, 0, a)$, so a is the amplitude of the shift ($0 \le a \le b$). The density that generates the gravitational potential (6) is

$$\rho = \frac{3M\psi}{4\pi b^3}\left[\psi^4 - \frac{10\tilde{a}^2\tilde{z}^2}{d^4} + \frac{5\tilde{a}^4\tilde{z}^4}{d^8\psi^4}\right]. \tag{9}$$

Here, we consider the shifted Plummer model with $a/b = 0.5$, whose potential and density maps in the meridional plane are shown in Fig. 3. We have integrated numerically several orbits in this potential, finding untrapped regular orbits, chaotic orbits, and resonantly trapped regular orbits. The top three panels of Fig. 4 show the traces in the SoS and the trajectories in the (R, z)-plane of three representative orbits, having the same values of E and L_z (their initial conditions are given in Table 1). Throughout this paper, as done for instance in Hunter (2005), we show only the $p_R > 0$ part of the SoS since it is sufficient for the purpose of illustrating the nature of an orbit. In the SoS, the consequents of the untrapped regular orbit (left-hand panel in Fig. 4) align on a 1D path since, as discussed in Section 2, the orbit conserves a third isolating integral of motion, which lowers the dimensionality of the phase-space manifold on which the orbit lies. The consequents of the chaotic orbit (middle panel in Fig. 4) fill a 2D region, meaning that a third isolating integral of motion does not exist. The right-hand panel of Fig. 4 shows the trace in the SoS of an orbit, which is regular (its trace in

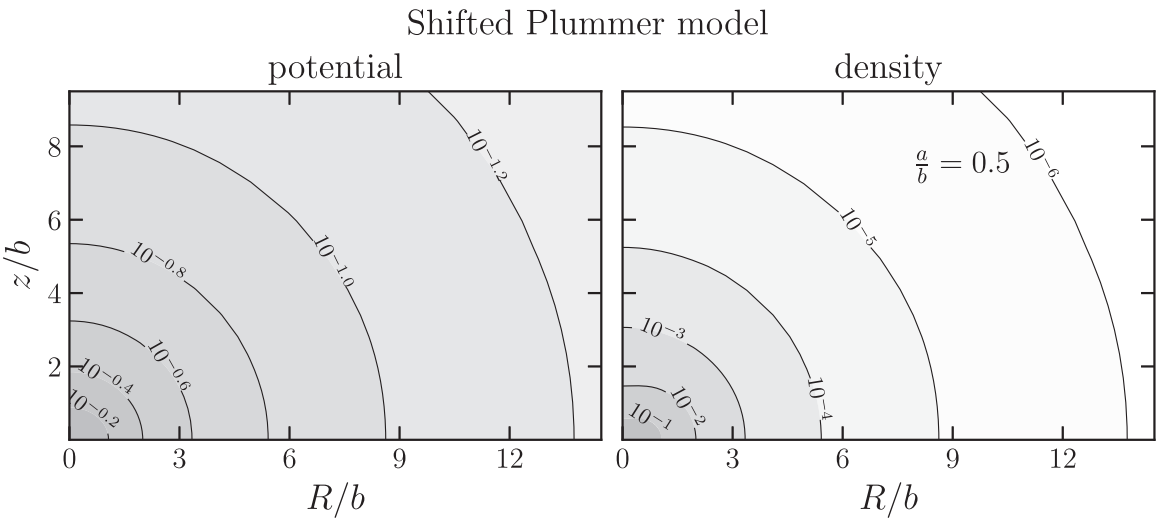

Figure 3. Left-hand panel: iso-potential contours in the (R, z)-plane of the shifted Plummer model (equation 6) with $a/b = 0.5$, labelled by the values of Φ/Φ_0, where Φ_0 is the central potential. Right-hand panel: iso-density contours of the same model as in the left-hand panel, labelled by the values of ρ/ρ_0, where ρ_0 is the central density.

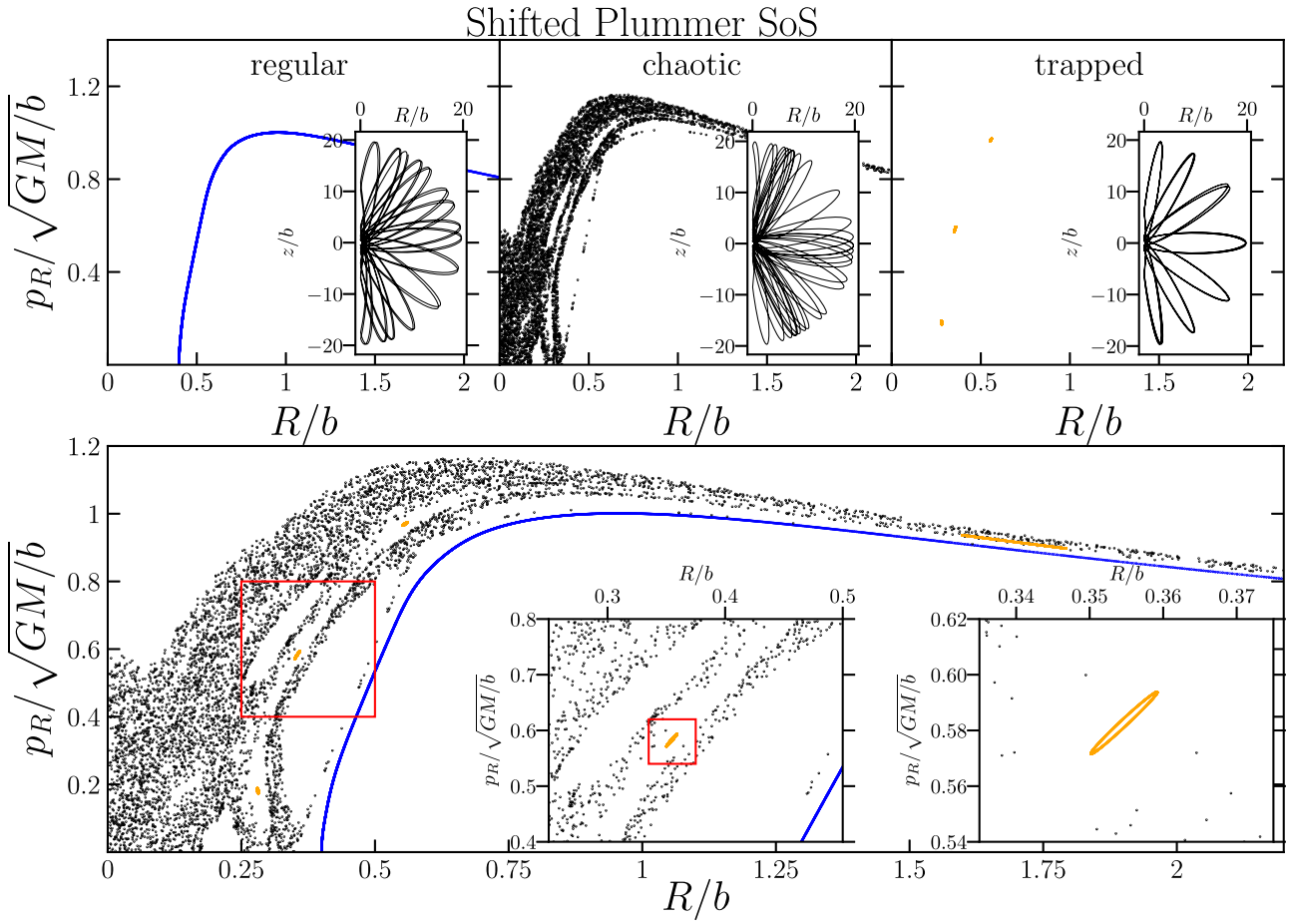

Figure 4. Top panels: traces in the SoS of a regular orbit (blue points, left-hand panel), a chaotic orbit (black points, middle panel), and a resonantly trapped orbit (orange points, right-hand panel) in the shifted Plummer potential (6) with $a/b = 0.5$. In each panel, the inset shows the trajectory of the corresponding orbit in the meridional plane. Bottom panel: traces of the same regular, chaotic, and resonantly trapped orbits as in the top panels, but plotted all in the same SoS. The left inset shows a zoomed-in view of the region marked with a red box in the main panel. The right inset shows a zoomed-in view of the region marked with a red box in the left inset. The ICs of the orbits are given in Table 1.

Table 1. Initial conditions in cylindrical coordinates, specific energy E, and vertical component of the specific angular momentum L_z of the regular, chaotic, and resonantly trapped orbits of Fig. 4 (ϕ is arbitrary and $p_\phi = L_z$). The orbits are integrated in the shifted Plummer potential (6) with $a/b = 0.5$.

	Shifted Plummer potential					
Orbit	R/b	z/b	$p_R/\sqrt{GM/b}$	$p_z/\sqrt{GM/b}$	$E/(GM/b)$	$L_z/\sqrt{GMb}$
Regular	0.4	0	0	1.413	−0.05	10^{-3}
Chaotic	0.35	0	0	1.428 69	−0.05	10^{-3}
Trapped	0.28	0	0.18	1.437 01	−0.05	10^{-3}

the SoS is one-dimensional), but trapped by resonance: the trace is a combination of circuits enclosing the points that represent, in the SoS, the parent resonant orbit.

The bottom panel of Fig. 4 shows in a single SoS the traces of the three orbits in the top panels. The trace of the resonantly trapped orbit is located within the resonant islands of the chaotic orbit (see insets in the bottom panel), while the trace of the regular orbit lies outside the region of the SoS occupied by the chaotic orbit. The boundary of resonant islands, representing the separation between resonantly trapped and chaotic orbits, are believed to correspond to the transition between a region of phase space influenced by only one resonance (within the island) and another region in which more than one resonance is important (outside the island). In the latter case, the star is scattered with no regularity, jumping from a resonance to another (a phenomenon known as resonance overlap; Chirikov 1979), which makes the orbit chaotic.

Having found chaotic orbits, we have demonstrated that, at least for $a/b = 0.5$, the shifted Plummer potential is non-integrable. More generally, this is also a proof that the complexification of a spherically symmetric model does not necessarily produce an integrable axisymmetric potential.

4.2 Orbits in a Miyamoto–Nagai potential

Let us consider the MN potential

$$\Phi(R, z) = -\frac{GM}{\sqrt{R^2 + \left[a + \sqrt{b^2 + z^2}\right]^2}}, \tag{10}$$

where a and b are, respectively, the model's scale radius and scale height, and M is the total mass of the system. The potential (10) is typically used to describe the disc components of spiral galaxies since it produces the disc-like density distribution

$$\rho(R, z) = \frac{b^2 M}{4\pi} \frac{aR^2 + \left[a + 3\sqrt{z^2 + b^2}\right]\left[a + \sqrt{z^2 + b^2}\right]^2}{\left[R^2 + \left(a + \sqrt{z^2 + b^2}\right)^2\right]^{\frac{5}{2}} \left(z^2 + b^2\right)^{\frac{3}{2}}}. \tag{11}$$

As shown by An & Evans (2019), given a spherical potential $\Phi(r)$, the MN substitution that maps

$$r \to \sqrt{R^2 + \left[a + \sqrt{b^2 + z^2}\right]^2} \tag{12}$$

produces oblate models with analytic density–potential pairs (see also Nagai & Miyamoto 1976; Satoh 1980). In this sense, the potential (10) is the generalization of the point mass potential. The MN potential (10) is of particular interest since its limiting cases for $b = 0$ and $a = 0$ are both integrable. When $b = 0$, equation (10) reduces to the Kuzmin disc (Kuzmin 1956; Toomre 1963), known to be of the Stäckel form. When $a = 0$, the MN potential becomes the classical Plummer sphere.

As in Hunter (2005), we study the orbits in a MN model with $a = b$, whose potential and density maps in the meridional plane are shown in Fig. 5. The case considered is a significantly, but not highly flattened oblate model. While Hunter (2005) in his exploration did not find chaotic orbits in the $a = b$ MN potential, we did find chaotic orbits in the very same potential. A selection of three of these orbits, whose initial conditions are given in Table 2, is shown in Fig. 6. The orbit in the left-hand panel has $|L_z|/L_{\rm circ}(E) = 4.57 \times 10^{-3}$, and the orbits in the middle and right-hand panels have $|L_z|/L_{\rm circ}(E) = 4.26 \times 10^{-3}$, where E is the orbit's energy and $L_{\rm circ}(E)$ is the magnitude of the angular momentum of a circular orbit in the equatorial plane with $R = 3(a + b)$ having energy E. Given that our orbits have approximately the same energy as the ones explored by Hunter (2005), we speculate that the reason why he did not find chaotic orbits is that his orbits have relatively high L_z ($|L_z|/L_{\rm circ} = 0.1$), while ours have $|L_z|/L_{\rm circ} \sim 10^{-3}$ (see also Section 5.2).

5 MASS CONTRIBUTIONS OF CHAOTIC AND REGULAR ORBITS TO STELLAR SYSTEMS

The results presented in Section 4 confirm and strengthen the general finding that, as a rule, non-Stäckel axisymmetric galactic gravitational potentials are non-integrable. Once ascertained the presence of chaotic orbits, the next step is to estimate how much they contribute to a given stellar system. In Section 5.1, we define the fractional mass contributions of chaotic and regular orbits to a stellar system of given DF, and we describe a statistical method to infer the expectation values of these quantities and the related uncertainties from a sample of orbits. Among regular orbits, we estimate separately the contributions of resonantly trapped and untrapped orbits. In Section 5.2, we present the results of a case study.

5.1 Definitions and estimates of the fractional mass contributions of orbit families

Let us consider a gravitational potential $\Phi(\mathbf{x})$ and a DF $f(\mathbf{x}, \mathbf{v})$ of a tracer population confined by Φ, with finite total mass

$$M = \int f(\mathbf{x}, \mathbf{v}) \mathrm{d}^3\mathbf{x} \mathrm{d}^3\mathbf{v}, \tag{13}$$

where the integral is extended to the entire phase space. Called $\mathcal{V}_{\rm c}$ the volume of phase space filled by chaotic orbits, the fractional contribution of chaotic orbits to the total mass is

$$\xi_{\rm c} \equiv \frac{M_{\rm c}}{M}, \tag{14}$$

where

$$M_{\rm c} = \int_{\mathcal{V}_{\rm c}} f(\mathbf{x}, \mathbf{v}) \mathrm{d}^3\mathbf{x} \mathrm{d}^3\mathbf{v} \tag{15}$$

is the mass contributed by chaotic orbits. Clearly, the fraction $\xi_{\rm c}$ depends both on the gravitational potential and on the tracers' DF. A

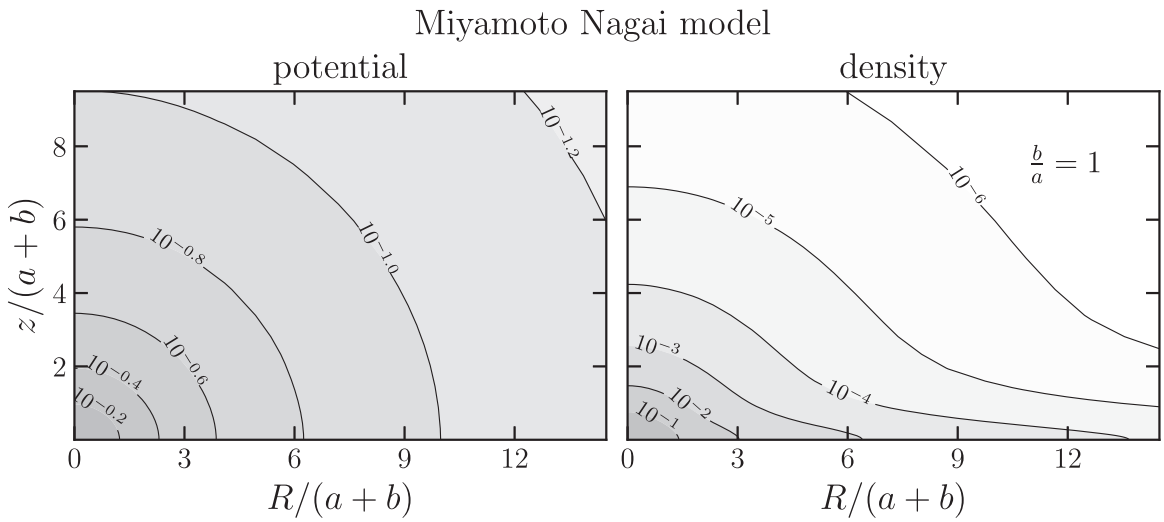

Figure 5. Left-hand panel: iso-potential contours in the meridional plane of a MN model with $a = b$, labelled by the values of Φ/Φ_0, where Φ_0 is the central potential. Right-hand panel: iso-density contours in the meridional plane of the same MN model as in the left-hand panel, labelled by the values of ρ/ρ_0, where ρ_0 is the central density.

Table 2. Same as Table 1, but for the chaotic orbits shown in Fig. 6, integrated in the MN potential (equation 10) with $a = b$.

orbit	$R/(a+b)$	$z/(a+b)$	$p_R/\sqrt{GM/(a+b)}$	$p_z/\sqrt{GM/(a+b)}$	$E/[GM/(a+b)]$	$L_z/\sqrt{GM(a+b)}$
MN1	0.05	0	0	−1.3629	−0.05	0.01
MN2	47.5482	−85.3202	−0.011 949	0.015 5498	−0.01	0.01
MN3	12.2099	−31.158	−0.076 7776	0.181 772	−0.01	0.01

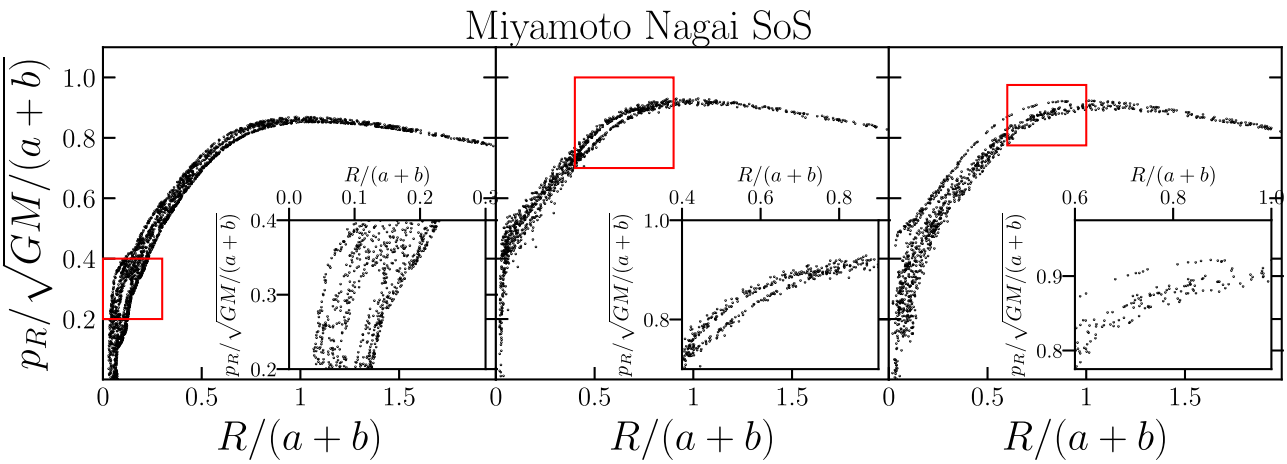

Figure 6. Traces in the SoS of three chaotic orbits in a MN potential with $a = b$. The initial conditions of these orbits (MN1, MN2 and MN3, from left to right) are given in Table 2. The insets show zoomed-in views of the red boxes in the corresponding main panels.

special case is the one in which the system is self gravitating, so that $\nabla^2\Phi = 4\pi G\rho$, where

$$\rho(\mathbf{x}) = \int f \mathrm{d}^3\mathbf{v}. \tag{16}$$

In the latter case, ξ_c is unique for given f, but not for given ρ. Two self-gravitating systems can have the same ρ (and thus the same Φ), but different DFs: ξ_c is in general different for each of these DFs. ξ_c can be estimated by extracting N orbits from f and counting how many of these N orbits turn out to be chaotic based on any orbit classification method.

Similarly to ξ_c, we define the fractional mass contribution of resonantly trapped orbits $\xi_\mathrm{t} \equiv M_\mathrm{t}/M$ with $M_\mathrm{t} = \int_{\mathcal{V}_\mathrm{t}} f \mathrm{d}^3\mathbf{x}\mathrm{d}^3\mathbf{v}$, where $\mathcal{V}_\mathrm{t}$ is the phase-space volume occupied by resonantly trapped orbits, and the fractional mass contribution of untrapped orbits $\xi_\mathrm{u} = 1 - \xi_\mathrm{c} - \xi_\mathrm{t}$. The fractional mass contribution of regular orbits (including both resonantly trapped and untrapped orbits) is $\xi_\mathrm{r} = \xi_\mathrm{t} + \xi_\mathrm{u}$.

In practice, to measure ξ_c, ξ_t, and ξ_u (and thus ξ_r), we proceed as follows. For given f and Φ, we extract N orbits from f, i.e. N sextuplets of phase-space coordinates ($\mathbf{x}$, $\mathbf{v}$) drawn from f. We integrate in time in the potential Φ the N orbits and classify them, finding N_c chaotic orbits, N_t regular resonantly trapped orbits and $N_\mathrm{u} = N - N_\mathrm{c} - N_\mathrm{t}$ regular untrapped orbits.

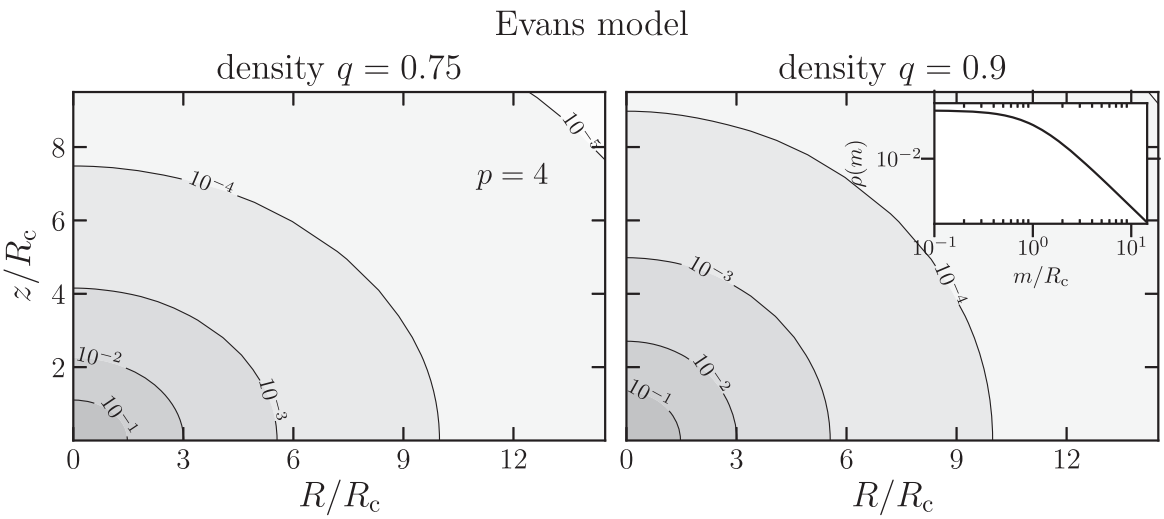

Figure 7. Left-hand panel: iso-density contours in the meridional plane of the density distribution (24) for $p = 4$ and $q = 0.75$, labelled by the values of ρ/ρ_0, where ρ_0 is the central density. Right-hand panel: same as the left-hand panel but for $q = 0.9$. The inset in the right-hand panel shows the density of the models as a function of the elliptical radius $m \equiv \sqrt{R^2 + z^2/q^2}$.

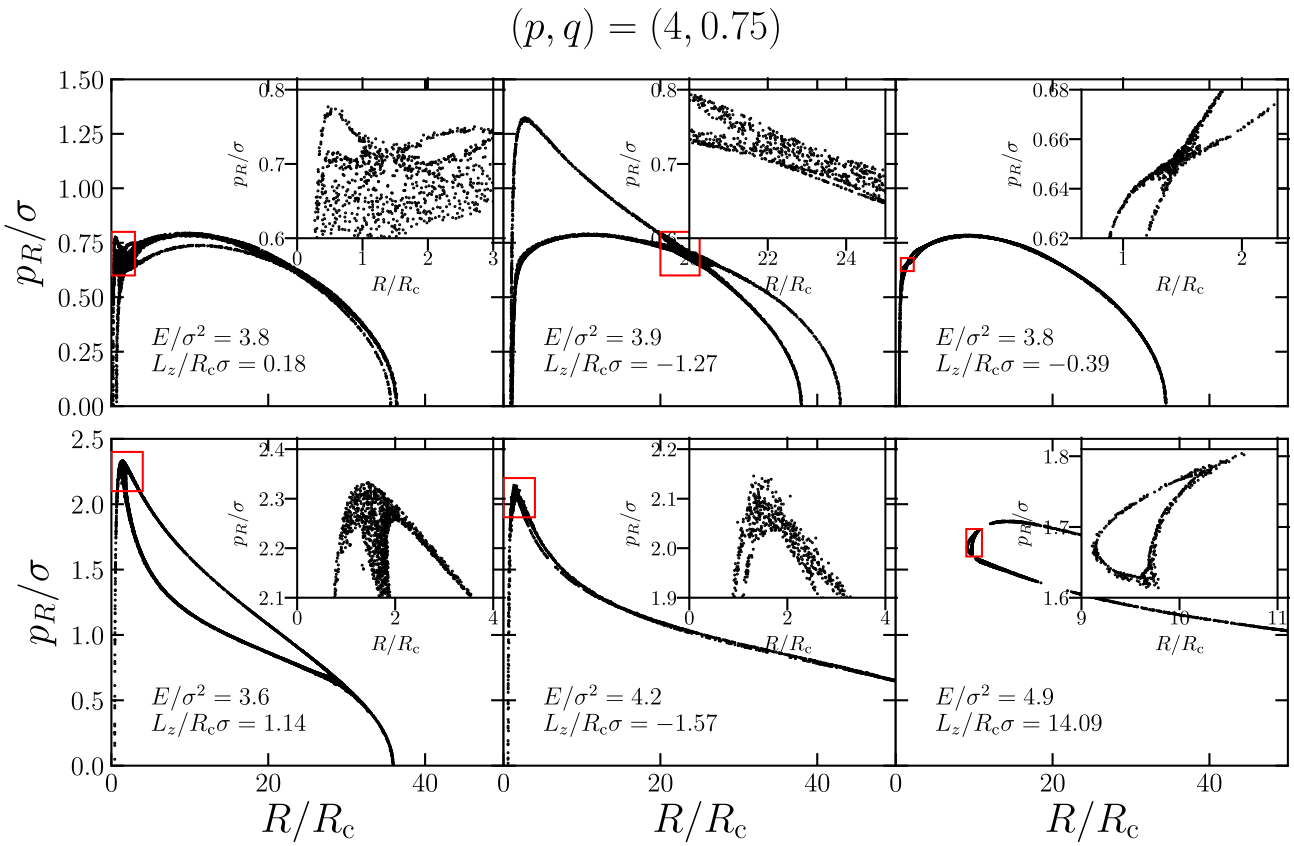

Figure 8. Traces in the SoS of a selection of six of the chaotic orbits found for the stellar system with gravitational potential (23) with $q = 0.75$. The inset in each panel shows a zoomed-in view of the region marked with a red box in the corresponding SoS.

Straightforward estimates of ξ_c, ξ_t, and ξ_u would be $\xi_c = N_c/N$, $\xi_t = N_t/N$, and $\xi_u = N_u/N$, but these numbers, though giving a rough measure of the fractional contributions of the different families of orbits, are not enough to describe in a statistically meaningful way the results of the numerical experiments, if we do not have a measure of the associated uncertainties. For instance, when $N_c = 0$, one would like to estimate an upper limit on ξ_c, which is expected to be more stringent for larger N.

We thus estimate ξ_c, ξ_t, and ξ_u, and the corresponding uncertainties $\delta\xi_c$, $\delta\xi_t$, and $\delta\xi_u$ using a Bayesian approach. The joint distribution of (N_c, N_t, N_u) is multinomial with parameters (N, ξ_c, ξ_t, ξ_u). We model

Table 3. Number of orbits, out of $N = 10\,000$, classified as chaotic (N_c), regular ($N_r = N_u + N_t$), untrapped (N_u), and resonantly trapped (N_t), and corresponding fractional mass contribution of each class of orbits (ξ_c, ξ_r, ξ_u, ξ_t) for a more flattened ($q = 0.75$) and a less flattened ($q = 0.9$) axisymmetric stellar system with ergodic Evans DF (21) with $p = 4$ and potential (23). The value of ξ_i, for i = c, r, u, and t, is given in the form $\widehat{\xi_i} \pm \delta\xi_i$, where $\widehat{\xi_i}$ and $\delta\xi_i$ are, respectively, the mean and the standard deviation of the posterior distribution of ξ_i.

	$q = 0.75$	$q = 0.9$
N_c	20	5
$N_r = N_u + N_t$	9980	9995
N_u	9419	9859
N_t	561	136
ξ_c	$(2.03 \pm 0.45) \times 10^{-3}$	$(5.33 \pm 2.31) \times 10^{-4}$
$\xi_r = \xi_t + \xi_u$	0.9980 ± 0.0012	$0.999\,47 \pm 0.000\,23$
ξ_u	0.9418 ± 0.0023	0.9858 ± 0.0012
ξ_t	$(5.61 \pm 0.23) \times 10^{-2}$	$(1.36 \pm 0.12) \times 10^{-2}$

the parameters (ξ_c, ξ_t, ξ_u) with a symmetric Dirichlet distribution with parameters (α, α, α), which implies that the marginal prior distribution of each component of (ξ_c, ξ_t, ξ_u) is a beta with parameters (α, 2α), corresponding to prior expected values $\xi_c = 1/3$, $\xi_t = 1/3$, and $\xi_u = 1/3$, which reflects our prior ignorance. Thanks to the conjugacy of the Dirichlet prior to the multinomial model, the posterior distribution of (ξ_c, ξ_t, ξ_u) is again Dirichlet with updated parameters ($\alpha + N_c$, $\alpha + N_t$, $\alpha + N_u$; see e.g. Robert 2007). A point estimator of (ξ_c, ξ_t, ξ_u) is given by the mean of the posterior distribution, that is

$$\left(\widehat{\xi_c}, \widehat{\xi_t}, \widehat{\xi_u}\right) = \left(\frac{\alpha + N_c}{3\alpha + N}, \frac{\alpha + N_t}{3\alpha + N}, \frac{\alpha + N_u}{3\alpha + N}\right). \tag{17}$$

The uncertainty associated to posterior estimates is quantified by considering the standard deviation of the marginal posterior distribution, given for ξ_c by

$$\delta\xi_c = \sqrt{\frac{(\alpha + N_c)(2\alpha + N - N_c)}{(3\alpha + N)^2(3\alpha + N + 1)}}, \tag{18}$$

and similarly for ξ_t and ξ_u.

Given that the fractional mass contribution of regular orbits is $\xi_r = 1 - \xi_c$ and that the marginal posterior distribution of ξ_c is a beta distribution $B(\alpha + N_c, 2\alpha + N_r)$, where $N_r = N_u + N_t$ is the number of regular orbits, the marginal posterior distribution of ξ_r is a beta distribution $B(2\alpha + N_r, \alpha + N_c)$. We take as point estimator of ξ_r the mean of the marginal posterior distribution

$$\widehat{\xi_r} = \frac{2\alpha + N_r}{3\alpha + N}, \tag{19}$$

and as uncertainty on ξ_r the standard deviation of the marginal posterior distribution,

$$\delta\xi_r = \sqrt{\frac{(2\alpha + N_r)(\alpha + N_c)}{(3\alpha + N)^2(3\alpha + N + 1)}}. \tag{20}$$

In what follows, we set $\alpha = 1/3$ which, if $N \gg 1$, corresponds to assigning little weight to the prior component when computing the posterior distribution.

To summarize, in order to quantify the fractional mass contributions of chaotic (ξ_c) and resonantly trapped (ξ_t) orbits to a non-spherical stellar system, either self-gravitating or immersed in an external gravitational potential, one should:

(i) know (analytically or numerically) the DF of the stellar system, because ξ_c and ξ_t depend on the DF, and not only on the total gravitational potential and the stellar density distribution;

(ii) extract from the DF a sample of N phase-space coordinates to be used as initial conditions for N orbits of the stellar system;

(iii) integrate the orbits in the total gravitational potential and classify them as untrapped regular, trapped regular, or chaotic, by means of any suitable classification method (for instance, inspection of the SoS or spectral analysis);

(iv) use Bayesian estimators, such as the ones provided by equations (17 and 18) to infer the expectation values of ξ_c and ξ_t and the associated confidence intervals.

5.2 A case study: a stellar system with ergodic DF confined by the flattened logarithmic potential

We now present examples of measurements of the fractional mass contributions defined in Section 5.1 for specific axisymmetric stellar systems. A natural choice could be to consider self-gravitating stellar systems with either the shifted Plummer or the MN gravitational potentials studied in Section 4. However, such systems, though having analytic density distributions (equations 9 and 11), as far as we know do not have easily tractable analytic DFs.[1] Though it is in principle possible to compute and use numerical DFs (e.g. Lynden-Bell 1962; Hunter & Qian 1993; Petač & Ullio 2019), here we prefer to avoid such a complication and focus on an exceptionally fortunate case in which density, potential, and DF have simple analytic expressions.

The stellar system here considered consists of a tracer population with DF f in an external potential Φ. As f, we take the ergodic DF of Evans (1993)

$$f(\mathbf{x}, \mathbf{v}) = f_0 \exp\left[-\left(\frac{pE(\mathbf{x}, \mathbf{v})}{\sigma^2}\right)\right], \tag{21}$$

where $E \equiv \Phi + K$ is the specific (i.e. per mass unit) energy, K is the specific kinetic energy, and

$$f_0 = \left(\frac{p}{2\pi^2 R_c^2 \sigma^2}\right)^{\frac{3}{2}} \frac{M}{q} \frac{\Gamma\left(\frac{p}{2}\right)}{\Gamma\left(\frac{p}{2} - \frac{3}{2}\right)} \tag{22}$$

normalizes the DF to the total mass M. The external potential is the flattened logarithmic potential (Binney 1981)

$$\Phi(R, z) = \frac{\sigma^2}{2} \ln\left(1 + \tilde{R}^2 + \frac{\tilde{z}^2}{q^2}\right), \tag{23}$$

where $\tilde{R} \equiv R/R_c$, $\tilde{z} \equiv z/R_c$, $q \leq 1$ is the minor-to-major axial ratio of the iso-potential surfaces, σ is the maximum circular speed, and R_c is the core radius (i.e. the distance from the centre within which the potential is roughly constant). We note that $\Phi(0, 0) = 0$, so $E \geq 0$ for all ($\mathbf{x}$, $\mathbf{v}$). The density distribution that generates the gravitational potential is everywhere positive when $q > 1/\sqrt{2}$. Since the DF (21) is ergodic, the density of the tracers stratifies on the iso-potential surfaces of (23).

Integrating the DF (21) over velocities, one finds that the tracers' spatial distribution is

$$\rho(R, z) = \frac{\rho_0}{\left(1 + \tilde{R}^2 + \tilde{z}^2/q^2\right)^{p/2}}, \tag{24}$$

[1]See Dejonghe (1986) for the analytic expression of the two-integral DF of the self-gravitating MN model.

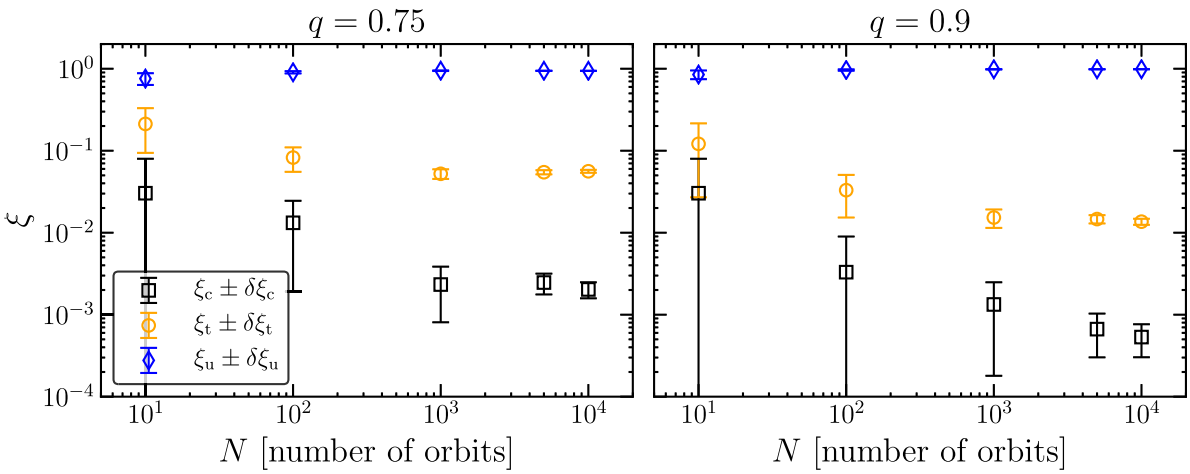

Figure 9. Estimates of the fractional mass contributions of chaotic (ξ_c; black squares with errorbars), trapped (ξ_t; orange circles with errorbars), and untrapped (ξ_u; blue diamonds with errorbars) orbits obtained by selecting random subsamples of N orbits among our samples of 10 000 orbits for the $q = 0.75$ (left-hand panel) and $q = 0.9$ (right-hand panel) Evans models.

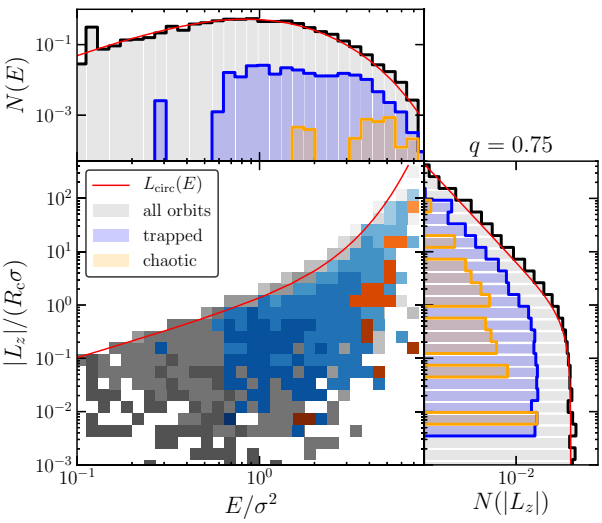

Figure 10. Distributions in the space of the orbital parameters E and L_z for our sample of orbits integrated in the flattened logarithmic potential (23) with $q = 0.75$. *Lower-left panel*: number density distribution of the explored orbits in the $(E, |L_z|)$ plane, for all orbits (grey), resonantly trapped orbits (blue), and chaotic orbits (orange): the darker the pixel's colour the higher the number density. The red curve indicates $|L_{circ}(E)|$ for circular orbits in the equatorial plane. *Upper panel*: differential energy distribution $N(E)$ for all orbits (grey), resonantly trapped orbits (blue), and chaotic orbits (orange), for the same sample of orbits as in the lower-left panel. The red curve indicates $N(E)$ as computed from the DF from which the sample of orbits is extracted (see Appendix B). *Right-hand panel*. Differential L_z distribution $N(|L_z|)$ for all orbits (grey), resonantly trapped orbits (blue), and chaotic orbits (orange), for the same sample of orbits as in the lower-left panel. The red curve indicates $N(|L_z|)$ as computed from the DF from which the sample of orbits is extracted (see Appendix B).

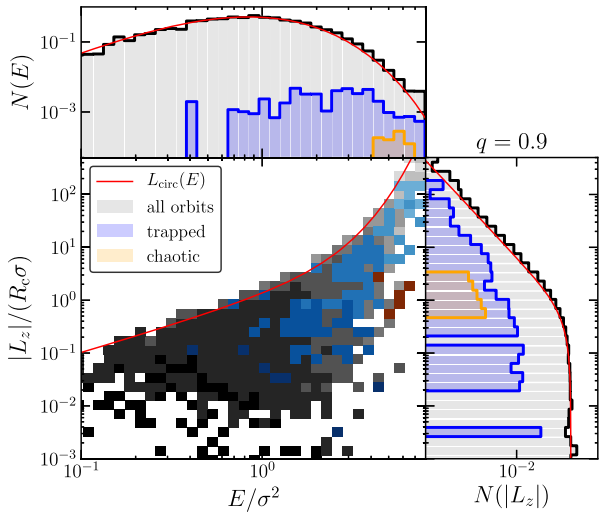

Figure 11. Same as Fig. 10, but for the sample of orbits integrated in the flattened logarithmic potential with $q = 0.9$.

with

$$\rho_0 = \frac{M}{\pi^{\frac{3}{2}} R_c^3} \frac{\Gamma(\frac{p}{2})}{q\Gamma\left(\frac{p}{2} - \frac{3}{2}\right)} \tag{25}$$

(Evans 1993). The tracers' density distribution (24) is a power law of slope p at large radii, while in the central regions a core of approximately constant density extends out of R_c. Since the DF is ergodic, the tracers' velocity distribution is isotropic and the second velocity moments are

$$\overline{v_R^2} = \overline{v_\phi^2} = \overline{v_z^2} = \frac{\sigma^2}{p}. \tag{26}$$

We focus on two specific models with $p = 4$, which differ only in the value of the potential's axial ratio q: a highly flattened model with $q = 0.75$, close to the minimum q allowed for consistency, and an almost spherical model with $q = 0.9$. Fig. 7 shows the isodensity contours of the $q = 0.75$ (left-hand panel) and $q = 0.9$ (right-hand panel) models. The small inset in the right-hand panel shows the density as a function of the elliptical radius $m \equiv \sqrt{R^2 + z^2/q^2}$, which is the same for both models (equation 24), with $\rho \propto m^{-4}$ when $m \gg R_c$. R_c and σ set the physical scales of the model.

For each model, we sample a set of $N = 10\,000$ orbit initial conditions from the DF (21), following the procedure[2] described

[2]This procedure does not exploit the fact that the DF is ergodic and can be used with any DF $f(\mathbf{x}, \mathbf{v})$.

in Appendix A. Each orbit is integrated in the potential (23) for $\approx 10^4 t_0$, with $t_0 \equiv R_c/\sigma$, and the SoS trace of each orbit is computed. For $p = 4$, the model's circularized half-mass radius is $r_h \simeq 2.2R_c$, so $t_0 \simeq r_h/(2.2\sigma)$. When the system is scaled to represent a typical massive elliptical galaxy with effective radius $R_{eff} \approx 10$ kpc and central stellar velocity dispersion $\sigma_0 \approx 250\,\mathrm{km\,s^{-1}}$ (e.g. section 5.4 of Cimatti, Fraternali & Nipoti 2019), assuming $r_h \approx R_{eff}$ and $\sigma \approx \sigma_0$, we get $t_0 \approx 18$ Myr. In all cases, the traces in the SoS are sampled with at least 1000 points.

For both $q = 0.75$ and $q = 0.9$, we find, among the explored orbits, a few chaotic orbits, which demonstrates that logarithmic potentials with these flattening parameters are non-integrable. Fig. 8 shows the SoS of a selection of six of the orbits classified as chaotic in the $q = 0.75$ model. To highlight the 2D structure of the manifold on which the consequents lie, the small insets in each panel show a zoom-in of a portion of the corresponding SoS. While we do find chaotic orbits, Richstone (1982) and Barnes (2001) did not find any chaotic orbit in the same logarithmic potential with $q = 0.75$, probably due to the low statistics of their sample of orbits. Richstone (1982) explored only 400 orbits, when, for instance, our results show that on average only one out of about 500 orbits is chaotic if the phase-space is populated with the DF (21) with $p = 4$. Barnes (2001) did explore even fewer orbits than Richstone (1982).

The number of chaotic (N_c), regular ($N_r = N_t + N_u$), resonantly trapped (N_t), and untrapped (N_u) orbits found for both $q = 0.75$ and $q = 0.9$ are reported in Table 3, together with estimates of the corresponding fractional mass contributions ξ_c, $\xi_r = \xi_t + \xi_u$, ξ_t, and ξ_u, obtained from equations (17–20) with $\alpha = 1/3$. While in both cases the regular orbits are by far the dominant family ($\xi_r \gtrsim 99.8$ per cent), the much rarer chaotic orbits contribute more to the more flattened system ($\xi_c \simeq 0.002$ for $q = 0.75$ and $\xi_c \simeq 0.0005$ for $q = 0.9$). The considered systems thus appear largely regular, with small contributions from chaotic orbits. For these chaotic orbits, our analysis (based on SoS traces obtained with long-time integration) does not provide information on the characteristic chaotic time-scale, that is the time over which the orbits starts showing a chaotic behaviour. It is then possible that a fraction of the found chaotic orbits are sticky (e.g. Maffione et al. 2015), i.e. that they behave similarly to regular orbits for relatively long time, before manifesting their chaotic nature. If this is the case, we would have found even smaller values of ξ_c if we had integrated the orbits for shorter times, more realistic for astrophysical applications. However, the adopted SoS orbit classification method forces us to consider long integration times, because a reliable classification requires that the orbit's trace in the SoS has a large number of consequents.

The mass contribution of resonantly trapped orbits is almost a factor of 30 higher than that of the chaotic orbits for both $q = 0.75$ and $q = 0.9$: in particular, the overall contribution is non-negligible in the case of the more flattened model ($q = 0.75$), in which about 6 per cent of the stellar mass is in resonantly trapped orbit. This is qualitatively[3] consistent with the results of Richstone (1982) who found that, in the same $q = 0.75$ logarithmic potential, ≈ 5 per cent of the orbits of his sample are resonantly trapped (note that Richstone adopts a different nomenclature in which the resonantly trapped orbits are called pipe orbits).

We note that we are able to provide estimates of ξ_c, ξ_t, ξ_u, and ξ_r with relatively small associated uncertainties (see Table 3), which means that the number of explored orbits ($N = 10\,000$ for each stellar system) is sufficient for our purposes. The estimates of the fractional mass contributions deteriorate with decreasing N. This is illustrated quantitatively by Fig. 9, showing, for both $q = 0.75$ and $q = 0.9$, the estimates of ξ_c, ξ_t, and ξ_u as functions of N, which we obtained by selecting random subsamples of N orbits among our samples of 10 000 orbits. As expected, the estimates for different N are statistically consistent, but the error bars on the fractional mass contributions shrink monotonically for increasing N.

In Figs 10 and 11, we show the 2D, joint distributions $n(E, |L_z|)$ for $q = 0.75$ and $q = 0.9$, respectively. $n(E, |L_z|)$ is such that $n(E, |L_z|)\mathrm{d}E\mathrm{d}|L_z|$ is the fraction of orbits with energy between E and $E + \mathrm{d}E$ and absolute value of L_z between $|L_z|$ and $|L_z| + \mathrm{d}|L_z|$. In each figure, the top panel shows the differential energy distribution $N(E)$, while the left-hand panel the differential L_z distribution $N(|L_z|)$. $N(E)\mathrm{d}E$ gives the fraction of orbits with energy between E and $E + \mathrm{d}E$. Similarly, $N(|L_z|)\mathrm{d}|L_z|$ is the fraction of orbits with absolute value of L_z between $|L_z|$ and $|L_z| + \mathrm{d}|L_z|$ (for details, see Appendix B). We have marked with different colours the contributions to the 1- and 2D distributions of the chaotic and resonantly trapped orbits. We note that as the energy increases, the relative contributions of the resonantly trapped and of the chaotic orbits increase while, especially for small values of $|L_z|$, their fractional contribution tends to remain approximately constant with $|L_z|$.

As an example of specific application, for instance within the framework of the study of the stellar streams generated by globular clusters (see Section 1), the Evans density distribution (24) can be interpreted as a simple model of the globular cluster system of a galaxy, whose gravitational potential is given by equation (23). Our analysis provides the fraction of these globular clusters that are expected to be on chaotic or trapped orbits, under the assumption that the velocity distribution of the globular cluster system is isotropic. Figs 10 and 11 suggest that these fractions should be similar for anisotropic velocity distribution, corresponding to DFs that either favour or disfavour high-$|L_z|$ orbits. The very small values found for ξ_c in the two explored models indicate that the fraction of GC streams dispersed by chaos would be negligible. The fraction of GC streams dispersed by separatrix divergence is not directly measured by our calculations, but ξ_t can be taken as an upper limit on this fraction, under the plausible assumption that there are more orbits belonging to resonantly trapped families than close to their boundaries.

6 CONCLUSIONS

We have addressed the problem of the integrability of a few families of axisymmetric potentials. Using numerical orbit integration, it is possible to show that a given potential is non-integrable, but of course it is not possible to demonstrate that it is integrable. We have added to the literature a few new cases of axisymmetric potentials that turn out to be non-integrable. These potentials belong to the families of shifted Plummer, MN, and flattened logarithmic potentials.

Given that chaotic orbits have been found for all (non-Stäckel) axisymmetric potentials in which they have been deeply looked for, an interesting question is how much these chaotic orbits contribute to stellar systems that are confined by these potentials. We have defined the fractional mass contribution ξ_c of chaotic orbits in stellar systems of given DF and proposed a simple but robust statistical method to estimate it from a sample of orbits. With the same approach, one can estimate also the fractional mass contributions of resonantly trapped regular orbits (ξ_t), of untrapped regular orbits (ξ_u) and of all regular orbits ($\xi_r = \xi_t + \xi_u$).

As a case study, we analysed two axisymmetric stellar systems with Evans DF confined by flattened logarithmic gravitational

[3]Richstone's sample of orbits is not extracted from a DF, so the comparison is not quantitative.

potentials with different values of the axial ratio q. The contribution of chaotic orbits is extremely small in both cases, but significantly higher in the more flattened ($q = 0.75$) system ($\xi_c = 0.0020 \pm 0.0005$) than in the almost spherical ($q = 0.9$) system ($\xi_c = 0.0005 \pm 0.0002$). In both cases, the mass contribution of resonantly trapped orbits is almost a factor of 30 higher than that of the chaotic orbits ($\xi_t = 0.056 \pm 0.002$ for $q = 0.75$ and $\xi_t = 0.014 \pm 0.001$ for $q = 0.9$). Most ($\gtrsim 94$ per cent) of the mass of these axisymmetric system is contributed by the standard untrapped regular orbits. The presented case study is particularly simple, because the considered axisymmetric stellar systems have analytic gravitational potential Φ, analytic ergodic DF f, and analytic spatial density ρ of the tracer population. However, we stress that the same analysis can be performed when the DF is not ergodic and/or one or more among Φ, f and ρ are not known analytically.

A fundamental step of our analysis is classifying orbits as chaotic and regular, and, among regular orbits, distinguishing resonantly trapped and untrapped orbits. In this paper, we have used as orbit classification technique the visual inspection of the SoS, but we stress that any technique for orbit classification can be used. Of course, visual inspection is impractical if one wants to systematically classify very large samples of orbits, which requires automatic classification algorithms (e.g. Carpintero, Maffione & Darriba 2014). We have seen that, from a geometrical point of view, orbits can be considered lower dimensional manifolds embedded in a higher dimensional space (the full phase space). To distinguish, at low computational cost, chaotic, and regular orbits one could estimate the intrinsic dimension of these manifolds (Mordohai & Medioni 2005) and build probabilistic models of a few selected prototypes (i.e. using generative topographic mapping; Bishop, Svensén & Williams 1998). Alternative methods based on the correlation integrals are also a viable way to estimate the dimensionality of the orbit in phase space (Carnevali & Santangelo 1984; Barnes 2001; Carpintero 2008) or of the trace in the SoS. However, determining the dimensionality of the orbit manifold is not enough to discriminate between untrapped and resonantly trapped orbits. Such a task requires either spectral methods (Binney & Spergel 1982; Carpintero & Aguilar 1998) or an algorithm able to classify topologically the traces in the SoS.

ACKNOWLEDGEMENTS

We are grateful to J. Binney, J. Magorrian, and B. Nipoti for helpful discussions. We thank an anonymous referee for comments and suggestions that helped improve this work. RP thanks G. Sabatini and G. Porrino for useful suggestions, comments, and moral support.

DATA AVAILABILITY

The data underlying this article will be shared on reasonable request to the corresponding author.

REFERENCES

An J., Evans N. W., 2019, MNRAS, 486, 3915
Appell P., 1887, Ann. Math. Lpz., 30, 155
Barnes E. I., 2001, ApJ, 559, 736
Bienaymé O., Robin A. C., Famaey B., 2015, A&A, 581, A123
Binney J., 1981, MNRAS, 196, 455
Binney J., 2016, MNRAS, 462, 2792
Binney J., 2020, in Valluri M., Sellwood J. A., eds, Galactic Dynamics in the Era of Large Surveys, Vol. 353, Cambridge Univ. Press, Cambridge, p. 101
Binney J., Spergel D., 1982, ApJ, 252, 308
Binney J., Tremaine S., 2008, Galactic Dynamics: Second Edition. Princeton Univ. Press, Princeton, NJ
Bishop C. M., Svensén M., Williams C. K. I., 1998, Neural Comput., 10, 215
Bonaca A. et al., 2020, ApJ, 889, 70
Bovy J., 2014, ApJ, 795, 95
Butcher J. C., 1996, Appl. Numer. Math., 20, 247
Candy J., Rozmus W., 1991, J. Comput. Phys., 92, 230
Carnevali P., Santangelo P., 1984, ApJ, 281, 473
Carpintero D. D., 2008, MNRAS, 388, 1293
Carpintero D. D., Aguilar L. A., 1998, MNRAS, 298, 1
Carpintero D. D., Maffione N., Darriba L., 2014, Astron. Comput., 5, 19
Carter R., 1968, Commun. Math. Phys., 10, 280
Chirikov B. V., 1979, Phys. Rep., 52, 263
Cimatti A., Fraternali F., Nipoti C., 2019, Introduction to Galaxy Formation and Evolution: From Primordial Gas to Present-Day Galaxies. Cambridge Univ. Press, Cambridge
Ciotti L., Giampieri G., 2007, MNRAS, 376, 1162
Ciotti L., Marinacci F., 2008, MNRAS, 387, 1117
de Zeeuw T., 1985, MNRAS, 216, 273
de Zeeuw P. T., Lynden-Bell D., 1985, MNRAS, 215, 713
Dejonghe H., 1986, Phys. Rep., 133, 217
Evans N. W., 1993, MNRAS, 260, 191
Fardal M. A., Huang S., Weinberg M. D., 2015, MNRAS, 452, 301
Forest E., Ruth R. D., 1990, Physica D Nonlinear Phenom., 43, 105
Gaia Collaboration, 2018a, A&A, 616, A1
Gaia Collaboration, 2018b, A&A, 616, A12
Gaia Collaboration, 2020, A&A, 649, A1
Greiner J., 1987, Celest. Mech., 40, 171
Greiner J., 1990, Celest. Mech. Dyn. Astron., 50, 387
Hagen J. H. J., Helmi A., Breddels M. A., 2019, A&A, 632, A99
Hastings W. K., 1970, Biometrika, 57, 97
Helmi A., 2004a, MNRAS, 351, 643
Helmi A., 2004b, ApJ, 610, L97
Helmi A., White S. D. M., 1999, MNRAS, 307, 495
Henon M., Heiles C., 1964, AJ, 69, 73
Hunter C., 2003, Disk-Crossing Orbits, Vol. 626, Springer, Berlin, p. 137
Hunter C., 2005, Ann. New York Acad. Sci., 1045, 120
Hunter C., Qian E., 1993, MNRAS, 262, 401
Kordopatis G. et al., 2013, AJ, 146, 134
Kuzmin G., 1956, Astron. Zh., 33, 27
Lynden-Bell D., 1962, MNRAS, 123, 447
Lynden-Bell D., 2000, MNRAS, 312, 301
Lynden-Bell D., 2003, in Thompson M. J., Christensen-Dalsgaard J., eds, Stellar Astrophysical Fluid Dynamics. Cambridge Univ. Press, Cambridge, p. 369
Maffione N. P., Gómez F. A., Cincotta P. M., Giordano C. M., Cooper A. P., O'Shea B. W., 2015, MNRAS, 453, 2830
Maffione N. P. et al., 2018, MNRAS, 478, 4052
Majewski S. R. et al., 2017, AJ, 154, 94
Mestre M., Llinares C., Carpintero D. D., 2020, MNRAS, 492, 4398
Metropolis A. W., Rosenbluth M. N., Teller A. H., Teller E., 1953, J. Chem. Phys., 21, 1087
Miralda-Escude J., Schwarzschild M., 1989, ApJ, 339, 752
Miyamoto M., Nagai R., 1975, PASJ, 27, 533
Mordohai P., Medioni G., 2005, Proceedings of the 19th International Joint Conference on Artificial Intelligence. IJCAI'05. Morgan Kaufmann Publishers Inc., San Francisco, CA, p. 798
Nagai R., Miyamoto M., 1976, PASJ, 28, 1
Petač M., Ullio P., 2019, Phys. Rev. D, 99, 043003
Plummer H. C., 1911, MNRAS, 71, 460
Press W. H., Teukolsky S. A., 1992, Comput. Phys., 6, 188
Price-Whelan A. M., Johnston K. V., Valluri M., Pearson S., Küpper A. H. W., Hogg D. W., 2016, MNRAS, 455, 1079
Richstone D. O., 1982, ApJ, 252, 496
Robert C., 2007, The Bayesian Choice: From Decision-Theoretic Foundations to Computational Implementation. Springer Science & Business Media, Berlin

Roberts G. O., Gelman A., Gilks W. R., 1997, Ann. Appl. Probab., 7, 110
Rosenthal J. S., 2010, Optimal Proposal Distributions and Adaptive MCMC. CRC press, Boca Raton, FL
Sanders J. L., Evans N. W., Geringer-Sameth A., Dehnen W., 2016, Phys. Rev. D, 94, 063521
Satoh C., 1980, PASJ, 32, 41
Schwarzschild M., 1979, ApJ, 232, 236
Schwarzschild M., 1982, ApJ, 263, 599
Stäckel P., 1893, Math.Ann., 42, 537
Stuchi T. J., 2002, Braz. J. Phys., 32, 958
Toomre A., 1963, ApJ, 138, 385
Valluri M., Merritt D., 1998, ApJ, 506, 686
Whittaker E. T., Watson E. T., 1950, A Course of Modern Analysis. Cambridge Univ. Press, Cambridge
Yavetz T. D., Johnston K. V., Pearson S., Price-Whelan A. M., Weinberg M. D., 2021, MNRAS, 501, 1791
Yoshida H., 1990, Physics Lett. A, 150, 262
Zotos E. E., Carpintero D. D., 2013, Celest. Mech. Dyn. Astron., 116, 417

APPENDIX A: EXTRACTING ORBITS FROM A DISTRIBUTION FUNCTION

We extract N orbits with phase-space coordinates $\mathbf{w}_k \equiv \{x_k, y_k, z_k, v_{x,k}, v_{y,k}, v_{z,k}\}$, with $k = 1, ..., N$, from a DF $f(\mathbf{x}, \mathbf{v})$ using a Metropolis-Hastings (Metropolis et al. 1953; Hastings 1970) sampler. Here, we briefly describe the procedure.

(i) From a given point in the phase space $\mathbf{w}_l$, a new location $\mathbf{w}_{l+1}$ is sampled using as proposal distribution a multivariate Gaussian distribution $\mathcal{M}$ centered in $\mathbf{w}_l$. The covariance matrix $\mathbf{C}^2$ of $\mathcal{M}$ is given by (e.g. Roberts, Gelman & Gilks 1997; Rosenthal 2010)

$$\mathbf{C}^2 = \left(\frac{2.38}{d}\right)^2 (\boldsymbol{\sigma}^2 + \varepsilon \mathbf{I}), \tag{A1}$$

where $d = 6$ is the dimension of the phase space, $\mathbf{I}$ is the identity matrix, $\varepsilon = 10^{-8}$, and $\boldsymbol{\sigma}^2$ is the chain's empirical covariance matrix, whose (i, j)-element is

$$\sigma^2_{i,j} = \frac{1}{M_{\min}} \sum_{m=M-M_{\min}}^{M} (w_{i,m} - \overline{w_i})(w_{j,m} - \overline{w_j}), \tag{A2}$$

with M the current chain size. The empirical covariance matrix and $\overline{w_h}$ (i.e. the mean over the h-th parameter of $\mathbf{w}$) are constructed using only the chain's latest $M_{\min} = 10000$ steps, allowing the sampler to adapt to the local structure of the probability distribution, and a new covariance matrix is built every 1000 steps. The term $\varepsilon\mathbf{I}$ avoids $\mathbf{C}^2$ to collapse to zero, especially during the first chain's steps, where the empirical covariance matrix cannot be recovered.

(ii) At each draw, the quantity $P \equiv \min[1, f(\mathbf{w}_{l+1})/f(\mathbf{w}_l)]$ is computed. The proposal $\mathbf{w}_{l+1}$ is accepted if $P = 1$ and, in this case, the next chain step starts from $\mathbf{w}_{l+1}$. Otherwise, the new proposal is accepted only if $P > U$, with U drawn from a uniform distribution in the interval]0,1[.

(iii) To build a sample of N elements, we use a chain with N_{chain} steps, where $N_{\text{chain}} = N_{\text{burn-in}} + N\delta n$, because we eliminate the first $N_{\text{burn-in}}$ burn-in steps, and, of the remaining chain, we take one draw every δn iterations. In particular, we adopt $N_{\text{burn-in}} = 50\,000$ and $\delta n = 200$, which guarantees that the final sample does not contain duplicate elements and that the sample's auto correlation is sensibly lowered.

APPENDIX B: USEFUL FORMULAE

Here, we report the expressions of the differential energy distribution and of the differential L_z distribution computed from the DF (21), which are shown in Figs 10 and 11.

The differential energy distribution is (Binney & Tremaine 2008)

$$N(E) = f_{0,E} \exp\left[-\frac{pE}{\sigma^2}\right] g(E;\sigma), \tag{B1}$$

where g is the non-normalized density of states, defined as

$$g(E;\sigma) = \int_0^{m_{\max}} m^2 \sqrt{\left[\frac{2E}{\sigma^2} - \ln(m^2+1)\right]}\,\mathrm{d}m, \tag{B2}$$

with

$$m_{\max} = \sqrt{\exp\left(\frac{2E}{\sigma^2}\right) - 1}, \tag{B3}$$

i.e. the root of the radical in equation (B2), and

$$f_{0,E} = \frac{2^{5/2} p^{3/2}}{\sigma^2 \pi} \frac{\Gamma\left(\frac{p}{2}\right)}{\Gamma\left(\frac{p}{2} - \frac{3}{2}\right)} \tag{B4}$$

is such that $\int_0^{+\infty} N(E)\mathrm{d}E = 1$.

In analogy with equation (B1), we define the differential L_z distribution (i.e. the number of orbits with $|L_z|$ in the interval $[|L_z|, |L_z| + \mathrm{d}|L_z|]$) as

$$N(|L_z|) = f_{0,L_z}\left[\int_0^{\infty} \frac{1}{(1+t^2)^{\frac{p-1}{2}}} \exp\left(-\frac{pL_z^2}{2\sigma^2 R_c^2 t^2}\right)\mathrm{d}t\right]\mathrm{d}|L_z|, \tag{B5}$$

and

$$f_{0,L_z} = \left(\frac{2p}{\pi}\right)^{\frac{1}{2}} \frac{p-3}{R_c \sigma} \tag{B6}$$

is such that $\int_0^{\infty} N(|L_z|)\mathrm{d}|L_z| = 1$.

This paper has been typeset from a TEX/LATEX file prepared by the author.